

This is an electronic reprint of the original article. This reprint may differ from the original in pagination and typographic detail.

Hierarchical Graphene-Dye Bilayers for Multimodal Optoelectronic Sensing and Decoupling of Complex Stimuli

Khatib, Muhammad; Rapoport, Shelley; Zohar, Orr; Mansour, Elias; Zheng, Youbin; Tang, Ning; Saliba, Walaa; Mulytin, Yana; Huynh, Tan-Phat; Haick, Hossam

Published in:
Advanced Materials Technologies

DOI:
[10.1002/admt.202200920](https://doi.org/10.1002/admt.202200920)

Published: 01/08/2022

Document Version
Final published version

Document License
CC BY

[Link to publication](#)

Please cite the original version:
Khatib, M., Rapoport, S., Zohar, O., Mansour, E., Zheng, Y., Tang, N., Saliba, W., Mulytin, Y., Huynh, T.-P., & Haick, H. (2022). Hierarchical Graphene-Dye Bilayers for Multimodal Optoelectronic Sensing and Decoupling of Complex Stimuli. *Advanced Materials Technologies*. <https://doi.org/10.1002/admt.202200920>

General rights

Copyright and moral rights for the publications made accessible in the public portal are retained by the authors and/or other copyright owners and it is a condition of accessing publications that users recognise and abide by the legal requirements associated with these rights.

Take down policy

If you believe that this document breaches copyright please contact us providing details, and we will remove access to the work immediately and investigate your claim.

Hierarchical Graphene-Dye Bilayers for Multimodal Optoelectronic Sensing and Decoupling of Complex Stimuli

Muhammad Khatib, Shelley Rapoport, Orr Zohar, Elias Mansour, Youbin Zheng, Ning Tang, Walaa Saliba, Yana Mulytin, Tan-Phat Huynh, and Hossam Haick*


Signals obtained by chemical or calorimetric sensors are highly coupled and complex, making it very challenging to precisely detect and discriminate between simultaneous stimuli. The development of sensors that provide multiple sensory outputs is a good way to tackle such a long-lasting challenge. Herein, a new design of multimodal sensors capable of generating both colorimetric and electrical sensory outputs is introduced. This is achieved by coupling two functional nanolayers, graphene (electrically active) and dyes (colorimetric) in which each layer can work either autonomously or in conjugation with the other sensing layer. It is shown that the interfacial interaction of graphene with the wide variety of dyes creates unique interfacial sensing sites for the detection of chemicals. This endows each sensor or sensor array, in the format of (opto)electronic nose, with a “fingerprint” of varying bonding possibilities, enlarging the spectrum of gas–sensor interactions. Furthermore, it is shown that the hierarchical nanobilayer structure allows the separation and discrimination of volatile organic compounds (VOCs) based on their diffusion kinetics. Taken together, the bilayer design qualifies as a superior sensor compared to unimodal devices by offering improved detection limits, wider dynamic ranges, and higher sensitivity and selectivity in the binary discrimination of a wide range of stimuli (temperature, relative humidity, and VOCs).

1. Introduction

The gas sensor market has primarily been dominated by applications in oil and gas, automotive, and other process industries.

M. Khatib, S. Rapoport, O. Zohar, E. Mansour, Y. Zheng, N. Tang, W. Saliba, Y. Mulytin, H. Haick
The Department of Chemical Engineering and Russell Berrie Nanotechnology Institute
Technion – Israel Institute of Technology
Haifa 3200003, Israel
E-mail: hhossam@technion.ac.il

T.-P. Huynh
Laboratory of Molecular Science and Engineering
Faculty of Science and Engineering
Åbo Akademi University
Porthaninkatu 3–5, Turku FI-20500, Finland

 The ORCID identification number(s) for the author(s) of this article can be found under <https://doi.org/10.1002/admt.202200920>.

© 2022 The Authors. Advanced Materials Technologies published by Wiley-VCH GmbH. This is an open access article under the terms of the Creative Commons Attribution License, which permits use, distribution and reproduction in any medium, provided the original work is properly cited.

DOI: 10.1002/admt.202200920

This may no longer be the case, especially with the recent boom in modern sensor applications for personal air-quality monitoring,^[1] pollution tracking and environmental monitoring,^[2,3] breath analysis for preventive health care,^[4,5] food safety,^[6] the internet of things,^[7,8] and more.^[9] However, due to the complexity of targeted real-life samples, which are composed of an enormous number of continuous and simultaneous signals (e.g., human breath includes mixtures of volatile organic compounds (VOCs) that are coupled with varying humidity and temperature values), the implementation of these applications becomes very challenging.^[5,10] Additionally, the cross-reactivity of most chemical and physical sensors where each sensor can respond to different stimuli in a similar way constitutes a further major limitation.^[11] These intricate challenges prevent the precise detection of chemical stimuli in complex environments. Therefore, it is appealing to develop highly informative sensing components that guarantee the

sensing and differentiation of target chemical stimuli from coupled physical and/or undesirable chemical interferents.^[5,7]

Highly informative (including multimodal, multivariable, multifunctional, etc.) sensors, which refer to smart sensors that provide an extended amount of information about their environment,^[9] can serve as a basis for sensing arrays with super-accurate detection of target stimuli.^[5,7,12–14] One interesting way to obtain such highly informative sensors is by combining multiple sensory outputs and methodologies into a single system. Since each chemical sensing approach has its own advantages and challenges, this would minimize drawbacks and enable faster verification of sensing information.^[14] The widely used cross-reactive electrical arrays are mostly based on simple “classic” single-output sensors.^[7] In these devices, the chemical modification/functionalization used for creating multiple recognition elements with unique fingerprints serves only for tuning the electrical/chemical properties of the conductive active component. For example, in the widely used monolayer-capped gold nanoparticle based arrays,^[15] the different organic monolayers act only as receptors for the recognition of VOCs, and they do not offer any other sensing functions. We speculated that developing “functional” modifications that contribute to further transduction opportunities, should be an interesting way for turning conventional electrical chemical sensors into highly informative.

This will eventually lead to sensor arrays with high discriminatory power allowing optimal detection and discrimination of multiple stimuli. This approach can be very simple, compared to the considerable costs and sophisticated designs often required for combining multiple devices and sensing modes.

Herein we introduce the synergetic hybridization of electronic and optoelectronic sensing in a highly informative single device, which can either work alone or in sensor arrays for artificial nose technologies. Specifically, by carefully designing graphene-dye nanobilayers, we could create chemical and physical multimodal sensors combining both colorimetric and electric transduction mechanisms at the single device level. The hierarchical nanometric design of the sensing bilayer was found critical for obtaining a synergetic multimodal sensing behavior and optimal extension and tuning of chemical responsiveness. We also found that the nanobilayer hierarchical structure provides additional chemical discrimination opportunities by manipulating the transport of VOCs toward the electrically active sensing layer. The combination of these sensing outputs and variables into a single device is expected to generate very powerful sensing arrays that take the electronic/optoelectronic nose technologies a step further toward more sophisticated and precise real-life applications.

2. Results and Discussion

2.1. Design of the Hierarchical Nanobilayer Sensing Platform

Figure 1a–c shows schematic illustrations of the design of the nanobilayer hierarchical structure made of reduced graphene oxide (rGO) and colorimetric dyes that can simultaneously provide colorimetric and electrical transduction mechanisms. Thanks to this design, we obtained a highly informative sensor capable of providing two sensing outputs and multiple sensing variables. The first output is provided by the colorimetric sensing mechanism which is related to color changes in the dye layer due to interaction with VOCs, humidity, or temperature variations. The second output is electrical which is obtained by the chemiresistive and thermistive behavior of the graphene-dye bilayers. Importantly, the electrical output provides multiple chemical sensing variables. Since the dye layer acts as a diffusion medium and manipulates the transport of VOCs toward the rGO layer, transient information which is based on gas exposure kinetics can be used to improve the discrimination capabilities between different VOCs. Accordingly, the electrical response to VOCs provides two variables: a steady state sensing variable and a transient sensing variable and both will be demonstrated in this work. Further explanation about the rationale behind the bilayer design can be found in Section S1, Supporting Information.

This proposed nanobilayer structure can be obtained using straightforward and cost-effective fabrication processes in which both layers are separately prepared but kept strongly coupled through careful interface optimization, as opposed to most composite/hybrid-based sensing materials that require sophisticated mixing and hybridization methods.^[3,16] The fabrication process starts with the deposition of graphene oxide (GO) nanolayer using spin-coating, followed by hydrazine reduction, providing an electrically active and transparent sensing layer of rGO (Figures S1 and S2, Supporting Information). This is followed

by the deposition of dye, which serves both as the colorimetric active sensing layers and as a modification to the surface of rGO for creating unique recognition elements. Fifteen different dyes (D2–D16) were used to prepare 15 different sensors (S2–S16, Section S2, Supporting Information). The remaining sensor, S1, refers to the reference sensor that only contains an rGO layer. We have optimized the dimensions of each layer to satisfy multiple contradicting requirements. On the one hand, thicker layers are required to obtain a desirable electrical resistance range, clear dye color, and efficient diffusion-based separation of VOCs. On the other hand, thinner layers are recommended for achieving higher gas sensitivity and faster response times. Notably, the transparency of rGO allows easy detection of color variations on exposure to gases and temperatures. Figure 1d shows a top-view SEM image of the rGO layer. Figure 1e shows top-view SEM images of selected graphene dye-bilayers, where varying nano-structured morphologies can be seen with the different dyes. We proposed that these varying structures are essential for obtaining pre-separation of gases that is based on their diffusion patterns, as is discussed later. Figures S3 and S4, Supporting Information, provide TEM images of rGO and a top-view SEM of additional sensors. Figure 1f shows photographs of the full sensing array consisting of multiple dyes. Modification of the interface of graphene using the bilayer design was verified by density functional theory (DFT) analysis, the results showing that the presence of dye molecules near rGO tunes its electronic properties, leading to positive/negative changes in the energy levels and band gap (Figure 1g,h). These interfacial modifications translate to different interface-gas interactions and eventually to tuned chemical sensitivities. Thus, each nanobilayer possesses a unique “fingerprint” in terms of sensing.

2.2. The Bilayer Structural Design and its Effect on Chemical Sensing

To shed light on and optimize the multimodal sensing performance of the nanobilayer structure, we ran different design experiments to examine the effect of bilayer dimensions (Figure 2a) and reduction time of GO on the sensing performance. Figure 2b,c shows that longer reduction times lead to lower sensitivities to acetic acid and hexylamine. One possible explanation might be the loss of sensing sites for interaction with gases upon heavy GO reduction. For structural design, we first showed that thinner layers of rGO (without a dye layer) generate higher response magnitudes (Figure 2d–e), and therefore we choose the lowest rGO thickness that could provide stable and detectable resistance values. This is a crucial factor for the bilayer design since the electrical response of thin rGO layers can be easily and efficiently tuned through interfacial coupling with different dyes, leading to significant effects on the sensing performance. Figure 2f–i shows the response ($\Delta R/R_0$ and $dR/R_0 dt$) of rGO-D6 bilayers with varying rGO thicknesses to acetic acid and hexylamine. As expected, thicker rGO layers gave lower responses and minimized the “fingerprint” of the dye, which could be explained by the lower effect of the dye on the bulk of thick rGO layers. Finally, we examined the effect of dye thickness on the sensing mechanism. Figure 2j–m shows that thinner dye layers generate

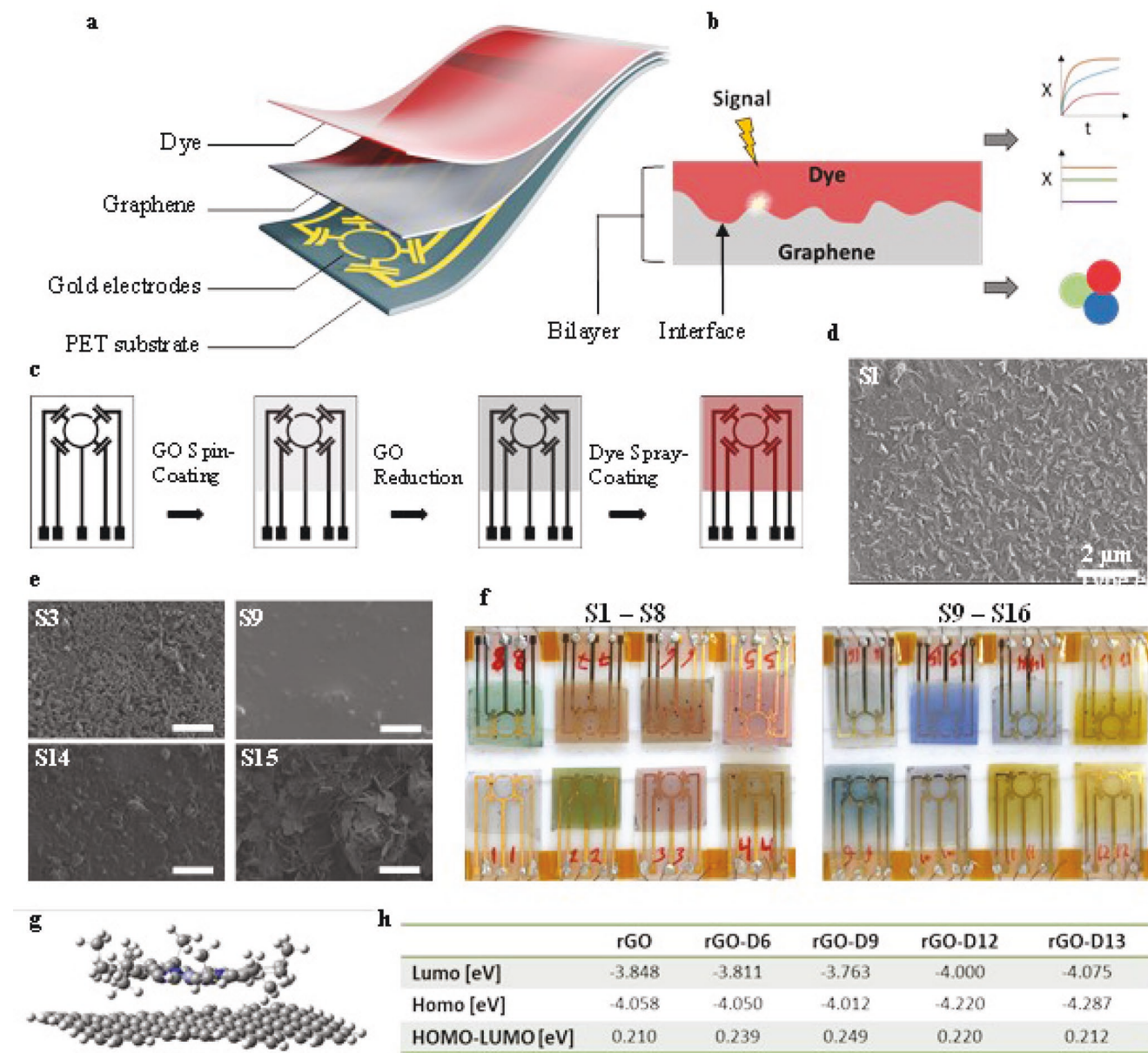


Figure 1. Design and fabrication of the sensing nanobilayer. a) Schematic illustration of the different layers found in each sensor. b) Schematic illustration of the extended multimodal sensing capabilities obtained in the bilayer design system, where chemical and physical signals can lead to colorimetric and electrical responses. Steady-state and time-dependent variables can be extracted from the electrical output. c) A briefed process of sensor fabrication. d) Top-view SEM images of the rGO layer and e) some representative examples of rGO-dye bilayers. f) Photographs of the sensing array showing all 16 sensors connected to the measurement board. g) Chemical structure of the rGO-D6 bilayer obtained using DFT. h) Variation of HOMO/LUMO levels obtained at the graphene-dye interface. Each representative dye provides a unique modification to the energy levels, which translates to tuned sensitivity toward gases.

larger responses, which could be explained by the fact that thicker dye layers might delay access of VOC molecules to the interface or block part of the sensing sites. This behavior was observed with both acetic acid and hexylamine, and it is highly important for achieving selective pre-separation of gases based on their diffusion patterns, which will be discussed in the next section. We extended these experiments by testing two other dyes, D5 and D13; the results are given in Figure S5, Supporting Information.

2.3. Response Kinetics and Reversibility of the Nanobilayer Sensor

Since the dye layer in the hierarchical nanobilayer design separates the sensing interface from the environment, it acts as a diffusion layer, leading to pre-separation and pre-concentration of VOCs based on their diffusion kinetics (Figure S6, Supporting Information). This is very similar to gas sensors that employ chromatography and microfluidics to separate

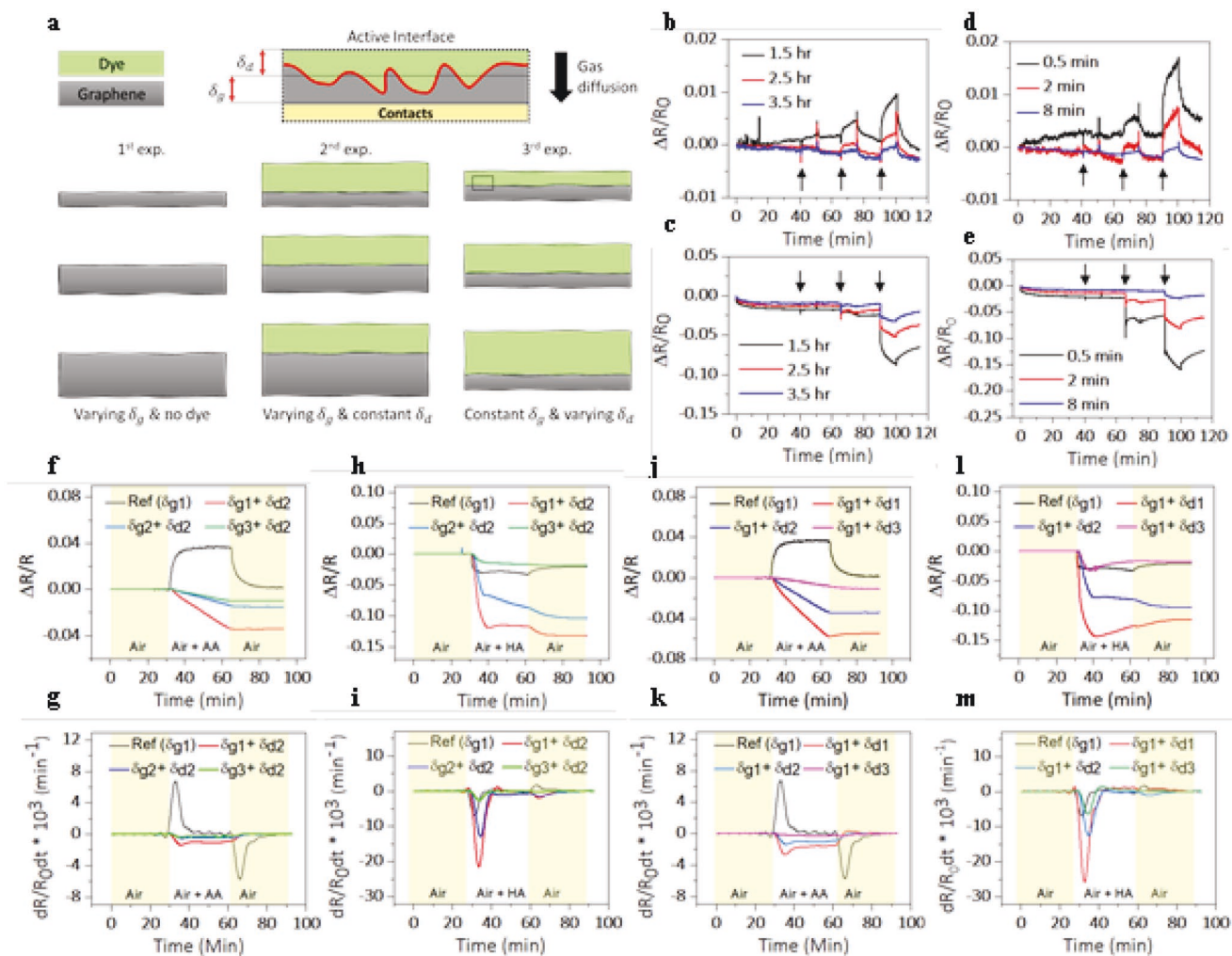


Figure 2. Study of the bilayer design and its effect on chemical sensing. a) Schema showing the interface structure and the 3 design experiments done in this section. b,c) Results of the reduction time experiment. Normalized resistance output from rGO-based sensors (without dyes) prepared using different reduction times (1.5, 2.5, and 3.5 h) on exposure to 3 concentrations of acetic acid (b) and hexylamine (c). d,e) Results of the first experiment described in Figure 2a–left. The graphs show the normalized resistance of sensors with varying rGO thicknesses on exposure to 3 concentrations of acetic acid (d) and hexylamine (e). The arrows mark the start of gas exposure. The times shown in the graph (0.5, 2, and 8 min) represent the delay before spin-coating (see Experimental Section), which translates to different thicknesses. Vacuum-based experiments were used here to allow faster responses and minimize diffusion-based processes. f–i) Sensing performance of rGO-D6 bilayers with varying thicknesses of the rGO layer (δg_1 , δg_2 , and δg_3) on exposure to 500 ppm acetic acid (f & g) and hexylamine (h & i). j–m) Sensing performance of rGO-D6 bilayers with varying thicknesses of the dye layer (δd_1 , δd_2 , and δd_3) on exposure to 500 ppm acetic acid (j & k) and hexylamine (l & m). The response is given in terms of the change in resistance versus time ($\Delta R/R_0$, f, h, j, & l) and the derivative of resistance versus time ($dR/R_0 dt$, g, i, k, & m).

different components in a mobile phase during the diffusion/transfer process.^[17] The hierarchy of the nanobilayer adds more dimensions to the electrical response and extends the extractable sensing variables, something that cannot be obtained by the simple electrical and colorimetric sensing components alone. The diffusion of VOC through a bilayer structure is further described by a non-dimensional partial differential equation in Section S3, Supporting Information. The effect of diffusion on manipulating the responses to VOCs is clear in Figure 2j,l, which shows how the increase in dye thickness slows down the response to gas exposure. **Figure 3a,b** shows the response of 4 sensors to acetic acid and hexylamine. Even though S1, S2, and S14 gave similar response magnitudes to acetic acid; they followed different kinetics, with S1 reaching

the final value first and S2 being the slowest in its response. Similar behavior was also noticed with hexylamine. Figure 3c shows the response of S5 to 90, 250, and 500 ppm hexanal and acetic acid. Both gases generated similar response magnitudes, with hexanal leading to a slower change in resistance. The distinctive response trends, marked in black and red arrows in Figure 3c, are caused by different sensing mechanisms and diffusion patterns. Accordingly, the combination of response kinetics (transient electrical variable) and final magnitudes (steady-state electrical variable) provides more sensing information and higher discriminatory power. To demonstrate this, Figure 3d shows the clustering of the 4 gases based on $\Delta R/R_{0, \max}$ and $dR/R_0 dt$ of S5. Figure S7, Supporting Information, shows the full data used in this example. Interestingly, the four

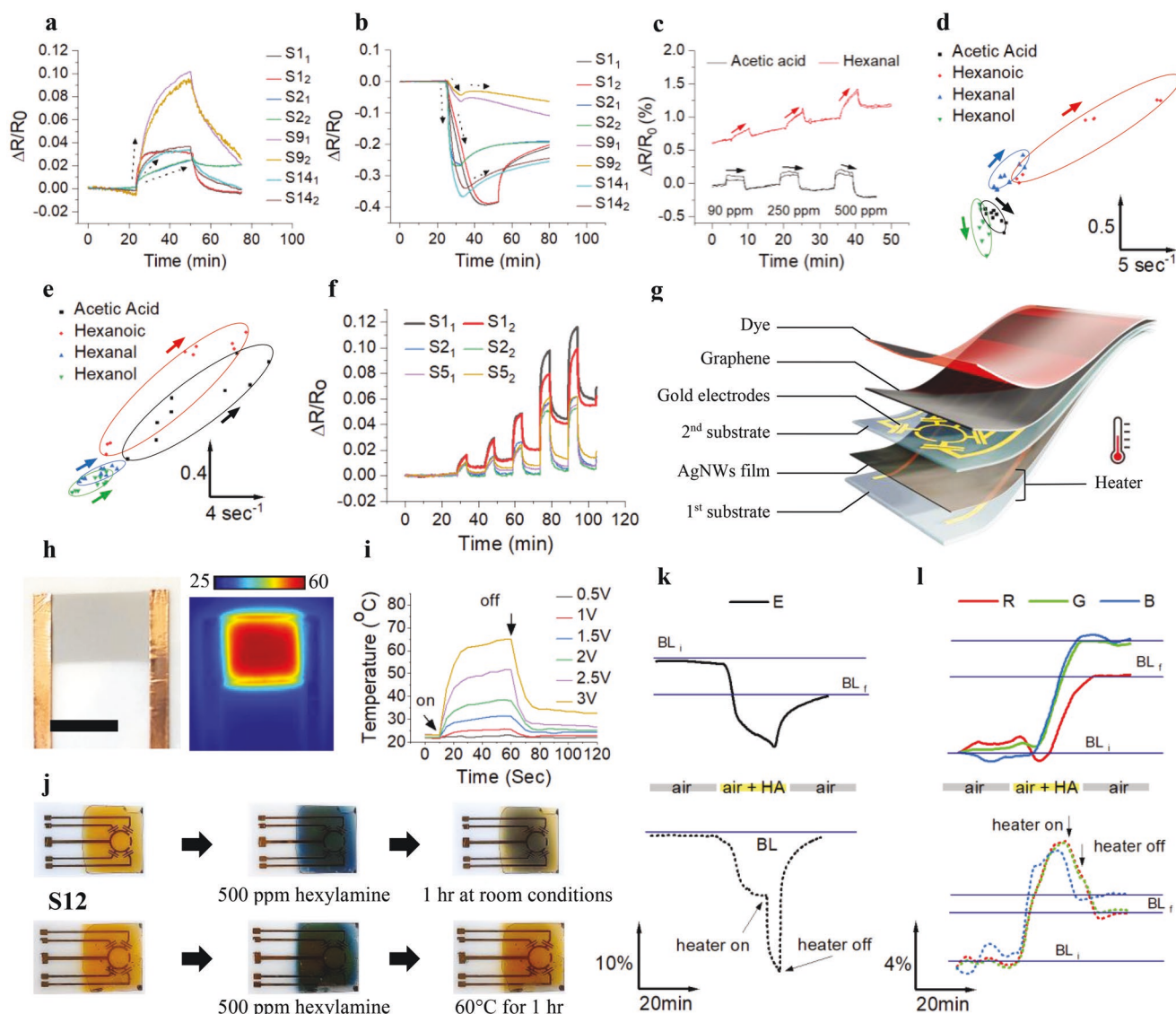


Figure 3. Response kinetics and reversibility. Responses of 4 types of sensors to a) 500 ppm acetic acid and b) 500 ppm hexylamine in a continuous flow experiment. Each sensor has its own response shape. Black arrows mark the trend (slop) of the response of each sensor. c) Response of S5 to 90, 250, and 500 ppm of hexanal and acetic acid in a vacuum-based experiment. While hexanal generated an increasing trend (marked by red arrows), acetic acid generated a decreasing trend (marked by black arrows). d) Discrimination between acetic acid, hexanoic acid, hexanal, hexanol, at concentrations of 90, 250, and 500 ppm based on both response kinetics and magnitude using only one sensor, S5. Y axis represents the magnitude of the response ($1000 \Delta R/R_b$), while x axis represents the derivative of resistance as a function of time ($1000 \cdot dR/R_0 dt$). The colored arrows mark increases in concentrations. e) Same discrimination as in (d) but using S1 instead of S5. f) The response of 3 different sensors (S_1 , S_2 , and S_5) to varying humidity levels (20, 40, 60, 80, and 100%). g) A schematic illustration showing the integration of heaters with the sensors. h) A photograph of AgNWs heater (left) and the corresponding thermal map obtained at 3 V (right). Scale bar: 1 cm. The temperatures in the thermal map are given in °C. i) Performance of the heater under different applied voltages. j) Photographs showing the reversibility of the colorimetric response of S12 after exposure to 500 ppm hexylamine using either ambient or heating conditions. k, l) The continuous electrical and colorimetric monitoring of the response and recovery of S8 after exposure to 500 ppm hexylamine, respectively, with and without heat. BL_i : initial baseline; BL_f : final baseline.

groups of gases can be separated with 100% accuracy using two lines in the $\Delta R/R_{b,max}$ and $dR/R_0 dt$ 2D plane. In comparison, S1 could not generate a similar separation capability due to the absence of hierarchy and/or dye-based chemical tuning (Figure 3e).

Sensor irreversibility is a major concern for colorimetric sensing, resulting from the strong analyte-dye interactions. One suggested solution is to use colorimetric sensing in disposable

arrays.^[18] This direction is acceptable provided the sensing arrays are cheap. Another highly interesting direction is the use of material design concepts to impart reversibility. Interestingly, in nanobilayer design, the existence of some dyes at the interface with graphene can improve the reversibility of the sensor. Figure 3f, for example, shows that S2 and S5 have better reversibility compared to S1 on exposure to different humidity levels. This is similar to the previously reported phenomena

where nanoscale heterostructures generate improved sensor recovery.^[19] Alternatively, we also used a smart circuit design to integrate heating components for accelerating chemical release and improving baseline regeneration (Figure 3g–i). Figure 3j shows the colorimetric reversibility of S12 after exposure to 500 ppm hexylamine under both ambient and heating conditions. The heat was very useful for the regeneration of S12's original color, while the ambient conditions did not provide sufficient energy for a similar regeneration. More examples and photographs can be found in Figure S8, Supporting Information. Figure 3k,l shows continuous electrical and colorimetric monitoring of S8's response and recovery after exposure to hexylamine, with and without heat. Once the heater is on, a big resistance change occurs, indicating temperature increase. Once it is off, the device goes back to its original baseline, indicating the release of chemicals. In comparison, the release under a continuous flow of air without heat did not result in complete recovery. The same behavior was seen by following the RGB signals of the sensor. The colorimetric reversibility obtained with some sensors is very interesting; notably, it was obtained with both acidic and basic chemicals.

2.4. Graphene-Dye Nanobilayers for Chemical and Physical Sensing Capabilities

One of the powerful advantages of the nanobilayer sensing platform is the possibility of the simultaneous use of colorimetric and electric sensing mechanisms for detecting multiple stimuli. To study and demonstrate these advantages, we considered a wide range of physical and chemical stimuli, including VOCs, humidity, and temperature. Starting from gas sensing, we studied 8 VOCs under concentrations ranging from 0–1000 ppm (see Experimental Section). Figure 4a shows the responses of rGO and 15 colorimetric dyes to vapors of hexanal. Significant colorimetric changes occurred in several dyes (marked in red). Images obtained from exposure to the other VOCs are provided in Figure S9, Supporting Information. A previously reported method was used to generate difference maps that visualize the sensors' colorimetric response.^[20] These pictures were scanned by a smartphone. Another example of colorimetric response is provided in Movie S1, Supporting Information, which shows S11–S13 changing colors when exposed to hexylamine. The simplicity of this method permits very accessible sensing that provides valuable real-time information about the chemical/physical environment. For electrical sensing, the responses, LOD, and the sensitivities of the sensors to different concentrations of VOCs are found in Figure S10 and Table S1, Supporting Information. Because of their chemical and physical properties each of the different gases and sensors generates its unique electrical sensing behavior (fingerprints), as demonstrated in Figure 4b,c. Interestingly, some dyes could even reverse the response trend; for example, S6/S3 response to hexanal compared to S1/S2 (Figure 4c). The same behavior was also noticed with acetic acid (Figure S11, Supporting Information). This strong tuning of the chemical sensitivity increases the discriminatory power of the final sensing array. Figure 4d shows simultaneous monitoring of the electrical

and colorimetric responses on exposure to different concentrations of acetic acid (left) and hexylamine (right). The magnitude of the colorimetric response is much bigger in both cases; however, the colorimetric LOD is higher. It is noteworthy that the colorimetric and electrical responses do not necessarily generate similar trends.

To shed light on the effect of dye on the response, we used DFT with a few representative sensors. The electronic density maps can be found in Figure S12, Supporting Information. Indeed, when acetic acid molecules are added to the model of the bilayer system, distinctive changes in energy levels and band gaps are obtained (Table S2, Supporting Information), that is, the “fingerprint” is characterized by a decrease in the band gap of rGO-D6/rGO-D9 and an increase for rGO-D12/rGO-D13. No change in the band gap of rGO on exposure to acetic acid. These results further support the effect of dyes on the electronic properties of the bilayer which translate to varied sensing behaviors.

Humidity and temperature are critical signals in almost every environment, and therefore it is vital to detect them precisely. Figure 4e,f shows the effect of dye on tuning the electrical sensitivity toward different humidity levels. Similar to previous work, the results show that the use of rGO-based materials for humidity sensing is promising.^[21] Some sensors, such as S3 and S6 provided higher sensitivities to variations in humidity levels compared to S1. Figure 4g summarizes the colorimetric response at different humidity values, with most of the dyes having no colorimetric response. The existence of humidity-insensitive chemistries is highly valuable for the final sensing array and its ability to neutralize the effect of humidity interference. We then focused on temperature sensing in the range of 10–70 °C. The rationale behind bimodal temperature sensing is based on using thermochromic dyes that change their color in response to the temperature. We used two different types of thermochromic dyes (Section S2, Supporting Information); D14 is based on a new polydiacetylene dye, similar to previously reported materials (Figure S13, Supporting Information).^[22] D15 & 16 are based on ternary thermochromic mixtures that include a dye, a developer, and a solvent, similar to commonly used thermochromic dyes.^[23] Movie S2, Supporting Information, shows S14's thermochromic response to temperature changes. Figure 4h,i shows the colorimetric and electrical responses of different dyes to temperature. Contrary to the evident graphene-dye coupling shown in electrical VOCs and humidity sensing (manifested as big response variations between bilayers made of different dyes), the electrical sensing of temperature showed negligible dependence on the type of dyes. Calibration for temperature sensing is given in Figure 4j, showing good linear performance in the studied range and a sensitivity value of $\approx 10^4$ ppm °C⁻¹. This value is also higher than many of the recently reported temperature sensors.^[13]

2.5. Multimodality for Improved Sensing Performance and Discrimination between Multiple Stimuli

The hierarchical bilayer sensor design provides many sensing advantages at both the single device and array levels. Starting from the electrical signal, the different dyes translate to tuned

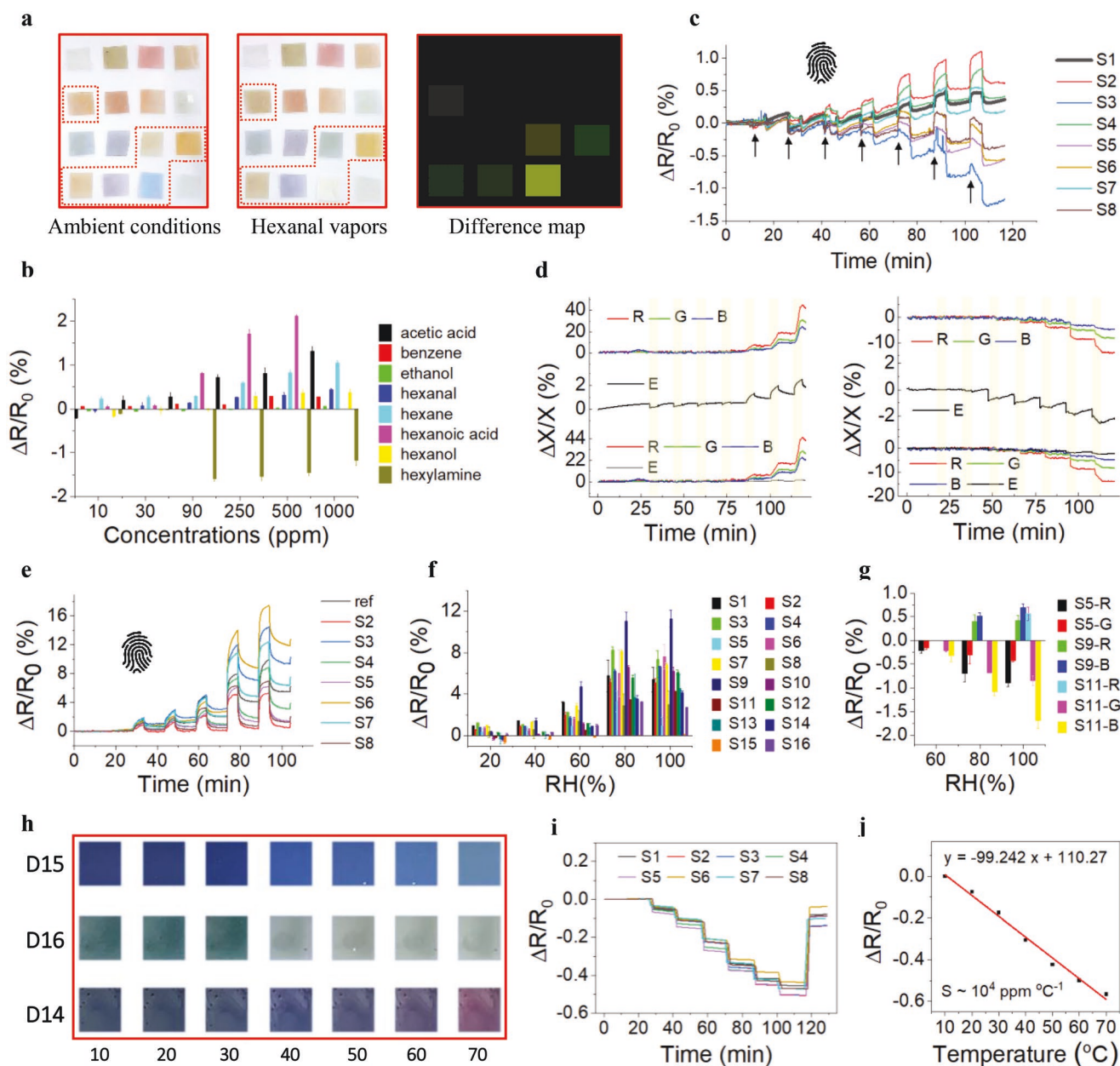
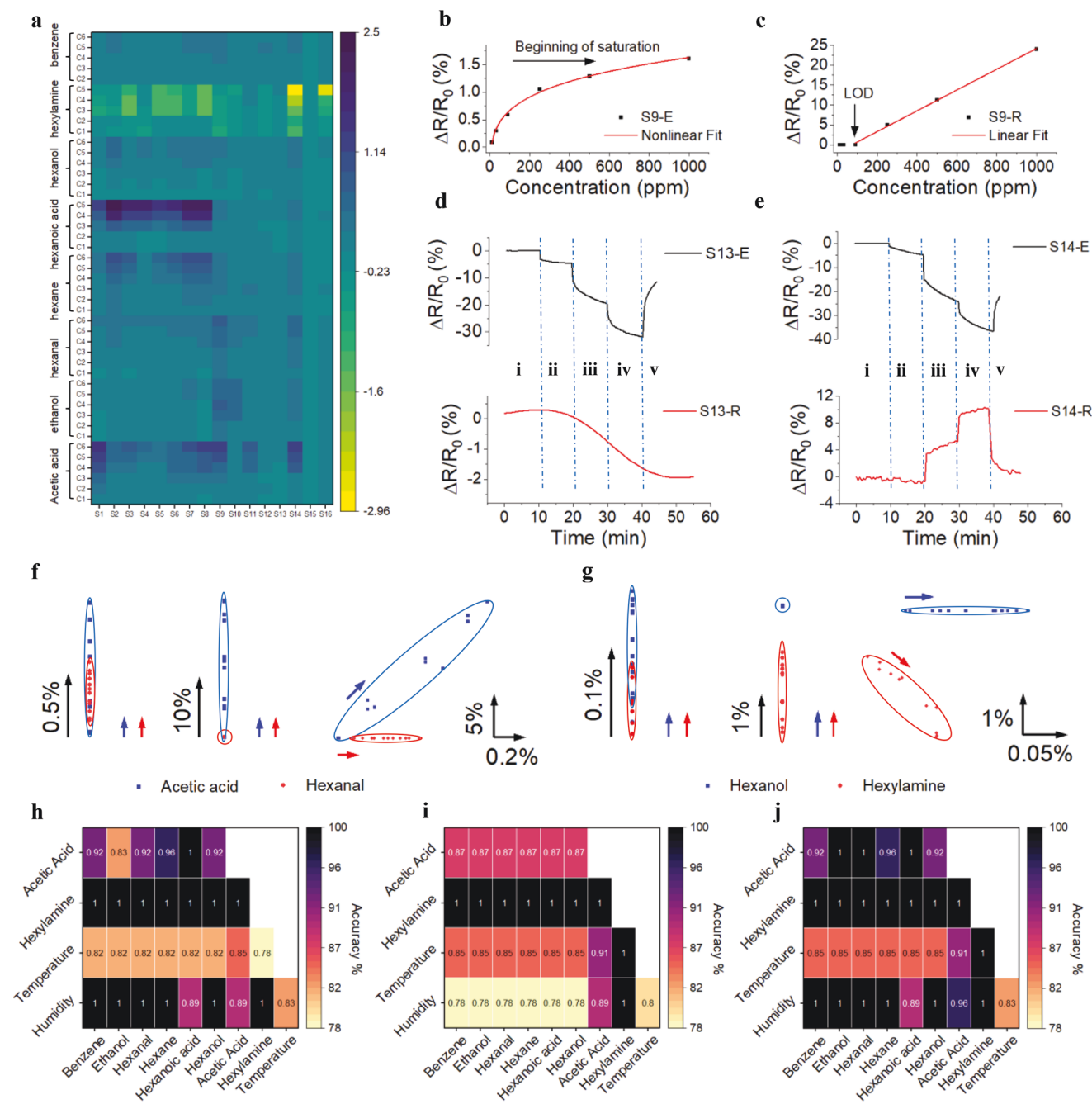


Figure 4. Multimodal colorimetric and electrical sensing. a) Smartphone-based detection of colorimetric dye response on exposure to vapors of hexanol. The difference map is shown on the right. b) Summary of the response of S8 to the different VOCs ($n = 3$). The sensor responds differently on exposure to each of the gases. c) Example of resistance change as a function of time during several cycles of vacuum and exposure to hexanol. Each arrow represents the beginning of one exposure step. There are 7 exposures in total that correspond to 0, 10, 30, 90, 250, 500, and 1000 ppm hexanol. d) Bimodal monitoring of hexylamine using S13 (right) and acetic acid S9 (left) involving both their colorimetric and electrical responses. There are 7 exposures marked in yellow bars to the following concentrations: 0, 10, 30, 90, 250, 500, and 1000 ppm. The white areas represent the vacuum steps. e) Response of several representative sensors to different values of relative humidity (20, 40, 60, 80, and 100%). f) Summary of the electrical responses of the bilayer sensors to different humidity levels (20, 40, 60, 80, and 100%, $n = 3$). g) Summary of the colorimetric response of the bilayer sensors to different humidity levels (60, 80, and 100%, $n = 3$). Only the dyes and humidity values that led to noticeable responses are shown. h) Photographs showing the colorimetric response of the thermochromic dyes (D14, D15, and D16) to temperatures ranging from 10 to 70 °C. i) Electrical response ($\Delta R/R_0$) to the same temperature values shown in (h). j) Calibration curve showing change in electrical resistance as a function of temperature. This was obtained by averaging the response of all the sensors.

chemical-electrical reactivity, providing very clear sensing “fingerprints”, as appears in the response patterns in Figure 5a where every sensor provides its unique behavior. This efficient electrical signal tuning facilitates the development of

cross-reactive sensor arrays for electronic nose technologies. When considering both electrical and colorimetric sensing, the developed sensors give two sensing outputs characterized by different dynamic ranges and sensitivities. Figure 5b,c shows



the electrical and colorimetric response of S9 to acetic acid. The electrical signal is more sensitive, with a lower LOD (1 ppm, Table S1, Supporting Information). However, the colorimetric signal is more sensitive in the high concentration regime and shows a more linear non-saturating behavior. Similar results were also seen with S12 responses to hexylamine (Figure S14, Supporting Information).

Multimodality can also improve discrimination between simultaneous stimuli/signals. For example, Figure 5d,e shows the response of S13 and S14 to simultaneous stimuli of hexylamine and temperature. The electrical signal alone cannot discriminate both stimuli since the response to temperature is dominant. However, when considering the colorimetric response, more information can be extracted. S13 has a continuously decreasing trend caused by hexylamine (S13 color does not respond to temperature). Moreover, S14 shows a clear response to temperature steps due to its strong thermochromic behavior. The use of all outputs together permits the detection and quantification of both stimuli simultaneously and importantly the decoupling of the chemical signal from temperature, which is impossible with the corresponding unimodal devices. We then showed that multimodal sensing can be highly valuable at the single sensor level. Figure 5f,g shows two examples of discrimination and clustering of responses to two different gases based on unimodal or bimodal sensing information coming from single sensors. In both cases, the electrical information can quantify both gases, but cannot discriminate them due to their overlapping responses. However, the colorimetric signal can selectively discriminate the two gases, but offers poor quantification. Importantly, when the bimodal output is considered, both selective discrimination and quantification of the two gases can be obtained. To systematically show the strength of bimodal sensing, we ran a binary discrimination test between the studied stimuli using either unimodal or multimodal performance (Figure 5h–j). Bimodal discrimination was more accurate than unimodal colorimetric or electrical discrimination. Noteworthy, these discrimination capabilities were demonstrated with both chemical and physical stimuli over a wide range of values.

Finally, as the information from multimodal sensing array is extensive, a principal component analysis (PCA) was applied to quantitatively estimate the discrimination between all the VOCs. We used either the electrical or bimodal signals for classification. Bimodal sensing is superior to the electrical sensing alone in all three models, linear, quadratic, and cubic (Table S3, Supporting Information). The electrical sensing alone could reach only 87.5% accuracy compared to 95.8% with the bimodal method. The PCA results suggest that bimodal sensing has the potential to provide more information to the sensing mechanism compared to unimodal electrical sensing, enhancing the discrimination between gases.

3. Conclusions

We have introduced a new design concept for combining multimodal and multifunctional sensing into a single highly informative device. By creating different rGO-dye nanobilayers, a cross-reactive sensing array has been generated with both

electrical and colorimetric sensing capabilities. It is possible to efficiently tune the chemical sensitivity of a thin rGO film by coupling it with another layer using a carefully designed bilayer structure. Strong coupling between the two layers was made obvious by significant variations/tuning in chemical response. The hierarchically layered structure also offered an interesting separation mechanism that helped in the classification of the different gases, based on their diffusion patterns and response kinetics. We have discussed many examples where the sensing performance of the multimodal sensing platforms is superior to unimodal sensing. The new array has been used to selectively detect and decouple a wide range of chemical and physical stimuli, including temperature, humidity, and VOCs. Finally, by careful circuit design, we have engineered controllable electrical and colorimetric reversibility to many sensors, which is highly valuable for reliable and long-term sensing. This work can be extended to include further sensing mechanisms, for example, the use of mechanoreceptors that change color in response to pressure can be coupled with electrically active films to allow bimodal pressure sensing in a single device. Additional transduction mechanisms, for example, gravimetric, can also be integrated with such a system to generate even more complex functions. We believe our work opens up new directions for the design of sophisticated and highly informative single components with multifunctional and multimodal sensing capabilities for the accurate discrimination of stimuli in complex environments.

4. Experimental Section

Preparation of GO: GO was prepared using a modified Hummer's method. Briefly, 2 g graphite was added to a mixture of concentrated H_2SO_4 (80 mL), $\text{K}_2\text{S}_2\text{O}_8$ (7 g), and P_2O_5 (5 g). The solution was heated to 80 °C for 5 h, then diluted with water, and left overnight before the product was collected by centrifugation. This solid was re-oxidized by another oxidation stage. For this purpose, the prepared product with NaNO_3 (1 g), was mixed with H_2SO_4 (95%, 48 mL) in a 250 mL flask. The mixture was stirred for 30 min in an ice-bath. Six grams of KMnO_4 were gradually added to the suspension, stirring vigorously. The ice-bath was removed, and the mixture was stirred at 35 °C for 5 h. Deionized water (60 mL) was slowly added to the paste also with vigorous stirring. The reaction temperature was increased to 98 °C, this temperature being maintained for 2 h. Finally, H_2O_2 (30%, 20 mL) was added. The mixture was washed with HCl (5% w/v) and deionized water several times to obtain GO, which was collected and vacuum-dried at 60 °C for 6 h. GO was purified using three centrifugation cycles.

Preparation of Dye Solutions: Detailed synthesis of dye 14 is provided in the Supporting Information. Solutions for dyes 1–14: 2 mg dye were dissolved in a mixture of chloroform/THF/DMF (1:0.8:0.2 volume ratio), followed by sonication for several minutes. This mixture was chosen to provide good solubility and PET wetting for obtaining homogeneous spray-coated films. For dyes 15 and 16, higher concentrations were used (providing thicker layers) to obtain high colorimetric signals. Thin films were highly transparent and not useful for the application. Therefore, for dye 15, 2 mg crystal violet lactone, 2 mg bisphenol A and 80 mg stearic acid were dissolved in 2 mL chloroform. For dye 16, 8 mg of dye 1,3-dihydro-1,3,3-trimethylspiro[2H-indole-2,3'-[3H]naphth[2,1-b][1,4]oxazine], 4 mg bisphenol A, and 80 mg tetradecanol were dissolved in 2 mL chloroform.

Sensor Fabrication: PET substrate with Ch/Au electrodes was washed and treated with O_2 plasma. 3-Aminopropyltriethoxysilane (APTES) was used to modify the surface of the substrate. The device

was cleaned in ethanol for 2 min under sonication. A drop of GO solution (2 mg mL⁻¹) was dropped and allowed to stay on the device for 2 min, and then spin-coated at 2000 rpm for 2 min, a step to get good GO deposition. The thickness of the GO layer was controlled by changing the time delay between spin-coating and drop-casting. 30 s, 2 min, and 8 min were used for examining the effect of thickness on the sensing performance. Reduction of graphene to GO was done by vapor reduction, using hydrazine monohydrate. The devices were loaded inside a glass bottle containing 250 μL hydrazine monohydrate, and the bottle was heated to 70 °C for 2.5 h. Reduction clearly showed a change in rGO film color from brown to black, which was monitored by transmittance measurements. This process generated a rough rGO layer with an average thickness of ≈100 nm, as measured by a surface profilometer. To examine the effect of reduction time on sensing, 1.5, 2.5, and 3.5 h were used. The device was kept under vacuum at 50 °C for 2 h. Finally, dye solutions were sprayed on top of the graphene using an air spray-gun at a pressure of 10 psi. The averaged thicknesses of the dye layers ranged from 200 to 400 nm for S2–S14 and ≈1–3 μm for S15 and S16. For controlling the dye layer thickness, different solution volumes (50, 200, and 800 μL) were sprayed. All devices were kept under vacuum before use. For sensor # 14, an additional polymerization process was required after spray-coating. Detailed description is provided in Section S2, Supporting Information.

Heater Fabrication and Use: AgNWs were prepared using a previously reported method. 10 mg AgNWs were dispersed in chloroform with 5% PMMA being added. The dispersion was sprayed on PET substrate and followed by heating at 100 °C for 10 min. The heater was then attached to the bottom of the gas sensor to produce a multilayered structure. The heaters were calibrated before the sensing experiments to determine which voltage provides the required temperature.

Gas/Humidity Sensing Experiments: The sensor array was connected to a board and placed into a ≈300 cm³ stainless-steel chamber for exposure to 8 different VOCs or humidity. The VOCs were hexane, hexanal, hexanol, benzene, hexylamine, and hexanoic acid, all of which have 6 carbons with different side groups. Acetic acid and ethanol were also tested to provide a comparison between the two and six carbon structures. Two types of experiments were usually run for gas sensing, one being based on vacuum whereas the other was based on a continuous flow (Section S4, Supporting Information). Vacuum-based experiments were run when multiple concentrations of gases were required because it was quick, whereas continuous flow experiments were used when the kinetics of the gas exposure were considered. In the vacuum-based system, the chamber was vacated for 45 min during the measurement of the resistance of the sensors to obtain a stable baseline. This stabilization step was followed by cycles of 5-min exposure and 10 min vacuum. In the continuous flow experiments, the sensors were exposed to N₂ for 45 min during measurement of the resistance of the sensors to obtain a stable baseline. This was followed by 30 min gas and then another 30 min of N₂ for release, being mainly used for a single gas exposure. For the preparation of suitable concentrations of VOCs/humidity, a computer-controlled bubbler was filled with the corresponding liquid before N₂ was bubbled through it. The resulting gas mixture (N₂ and organic vapor/humidity) was diluted to the desired concentrations.

Temperature Sensing Experiments: The sensor array was connected to a board and placed into a stainless-steel chamber of ≈300 cm³ with a thermocouple inside. The chamber was heated from the outside to obtain the required temperatures. The resistance of the sensors was measured for 1 min at each specific temperature.

Colorimetric Monitoring and RGB Signal Analysis: The regions of interests were manually selected, and a mask for each sensor was constructed (mask a). Using a threshold operation, the white background was highlighted. By selecting pixels in the vicinity of the region of interest, a “background mask” was constructed (mask b). The average & STD RGB values of the pixels were then measured inside the a) “mask” and the b) “background mask” at every frame. The “corrected RGB values were defined as the average R/G/B value measured in the region of interest, divided by that in the neighboring

background pixels. As the background pixels were supposed to be white, this was used to take care of incident light fluctuations. The blue channel also undergoes an empirically derived and constant (among all experiments) gamma correction with $\gamma = 1.7$ (corrected = measured^{1.7}).

Data and Statistical Analysis: All sensors were exposed to the studied stimuli three times ($n = 3$). Signals were pre-processed in MATLAB (2019b) by three steps. First, the resample function to resample the signal in constant time-steps; second, the function smoothdata to smooth the signal using a loess filter with a varying smoothing factor of 0.04–0.28, depending on the noise level; and third, detrending the signal using the detrend function with a varying polynomial degree of 2–4, depending on the trend of the signal. The response to each stimulus ($\Delta R/R_{b_i}$) was extracted from each processed signal (Section S5, Supporting Information). For gas sensing, the response to zero concentration was subtracted from the responses to the other concentrations for normalization.

Smartphone-based Detection of Colorimetric Responses: In this experiment, the colorimetric response to VOC exposure was measured. The different sensors (containing only the bilayer structure; no electrodes) were attached to a white Teflon substrate and exposed to different concentrations of VOCs in a closed chamber for 1 h. The array was scanned before and after exposure. Difference maps were created to visualize the response of each sensor to the VOCs. This was done using the following method: 1) The average difference value was calculated for each sensor by subtracting the RGB values from the two scans (before and after exposure), generating a 3D RGB difference vector for each sensor and each gas, $V_{si,gi} = (R_{si,gi}, G_{si,gi}, B_{si,gi})$, where si refers to sensor number i and gi refers to gas number i . 2) Another difference vector was generated from the average RGB difference obtained from the white Teflon background, $V_{bg,gi} = (R_{bg,gi}, G_{bg,gi}, B_{bg,gi})$. This was used as a reference for calibration and was subtracted from all the previous vectors, obtaining a new calibrated one, $V_{si,gi_cal} = (R_{si,gi}, G_{si,gi}, B_{si,gi}) - (R_{bg,gi}, G_{bg,gi}, B_{bg,gi})$. 3) The RGB range obtained in V_{si,gi_cal} was expanded to a new range of values from 0 to 255 for each color for contrast improvement, giving a new expanded vector, V_{si,gi_cal_exp} . The final RGB values ($R_{si,gi_cal_exp}, G_{si,gi_cal_exp}, B_{si,gi_cal_exp}$) characterizing each sensor and each exposure were used to create the difference image.

DFT Calculations: Gaussian 16 software was used to optimize the molecular structure, as well as the HOMO and LUMO energy of rGO, complexes of rGO and dyes, complexes of rGO-dye with acetic acid molecule, using a DFT method with dispersion correction APFD and the basis set 3–21G*.

Binary Discrimination Scores: The most discriminative features/sensors were identified based on their discrimination accuracy. The value indicates the ability to discriminate between groups of gases/signals. After plotting the responses of the sensor to different signals, if separate clusters (that correspond to each group) were obtained, this means that the sensor can discriminate between the gases. If the two groups overlap, then discrimination was low. By assigning a specific range of values to each group, the accuracy can be calculated by the portion of points found in the correct corresponding range. The highest accuracy was obtained when there were completely separate clusters. When using a unimodal system, the response vector and the assigned response range were 1D, whereas when using a bimodal system, the response vector and the assigned response range were 2D.

PCA Analysis: As the information from multimodal sensing method was extensive, PCA was applied to the data. To investigate quantitatively the discrimination ability, sensors 1–16 and the colorimetric sensors 9, 11, 12, 13, 14, and 16 were involved in two classification methods. The first was by using only the electrical signals, and the second was by using bimodal sensing. For the purpose of classification, only 3 concentrations were used: 90, 250, and 500 ppm. Support Vector Machine (SVM) was applied for classification, using the “Classification Learner” app in MATLAB (2019b). SVM has several types: linear, quadratic, cubic, and others, and was suitable for small datasets. Note, no cross-validation was implemented as the sample size was small, including only a single exposure per VOC, but the purpose of the

classification here was to show the ability of the system to differentiate between different VOCs. The colorimetric signal was not used alone because multiple gases did not show a colorimetric response in the range of concentrations used, and therefore the discrimination capabilities were expected to be low.

Supporting Information

Supporting Information is available from the Wiley Online Library or from the author.

Acknowledgements

This research received funding from the Phase-II Grand Challenges Explorations award of the Bill and Melinda Gates Foundation (OPPI109493) and Horizon 2020 ICT grant under the A-Patch project. National Institute of Health Research UK.

Conflict of Interest

The authors declare no conflict of interest.

Author Contributions

M.K. conceived the idea, designed the sensors, and planned the experiment. S.R. fabricated sensors and ran the gas sensing experiments. O.Z. and E.M. contributed to the analysis of the electrical and colorimetric data. Y.Z. did the temperature sensing experiments and heater fabrication. N.T. helped in the preparation and characterization of graphene. W.S. contributed to the design of measurement systems for exposure to chemical and physical stimuli. Y.M. helped in the structural characterization of the devices. T.-P.H. performed the DFT calculations. M.K. wrote the paper. O.Z., Y.Z., S.R., E.M., T.-P.H., and H.H. reviewed and edited the paper. H.H. supervised the project.

Data Availability Statement

Research data are not shared.

Keywords

chemical sensor, colorimetric sensor, graphene, multifunctional, multimodal

Received: June 7, 2022

Revised: July 5, 2022

Published online:

- [1] H. M. Fahad, H. Shiraki, M. Amani, C. Zhang, V. S. Hebbar, W. Gao, H. Ota, M. Hettick, D. Kiriya, Y.-Z. Chen, *Sci. Adv.* **2017**, *3*, e1602557.
[2] H.-E. Joe, H. Yun, S.-H. Jo, M. B. Jun, B.-K. Min, *Int. J. Precis. Eng. Manuf.-Green Technol.* **2018**, *5*, 173.

- [3] Y. Jian, W. Hu, Z. Zhao, P. Cheng, H. Haick, M. Yao, W. Wu, *Nano-Micro Lett.* **2020**, *12*, 71.
[4] a) S. Yao, P. Swetha, Y. Zhu, *Adv. Healthcare Mater.* **2018**, *7*, 1700889; b) S. Khan, S. Ali, A. Bermak, *Sensors* **2019**, *19*, 1230; c) O. Zohar, M. Khatib, R. Omar, R. Vishinkin, Y. Y. Broza, H. Haick, *View* **2021**, *2*, 20200172; d) H. C. Koydemir, A. Ozcan, *Annu. Rev. Anal. Chem.* **2018**, *11*, 127; e) T. P. Huynh, H. Haick, *Adv. Mater.* **2018**, *30*, 1802337; f) T. Yamada, H. Sugiura, H. Mimura, K. Kamiya, T. Osaki, S. Takeuchi, *Sci. Adv.* **2021**, *7*, eabd2013.
[5] M. Khatib, O. Zohar, H. Haick, *Adv. Mater.* **2021**, *33*, 2004190.
[6] G. Bülbül, A. Hayat, S. Andreescu, *Sensors* **2015**, *15*, 30736.
[7] R. A. Potyrailo, *Chem. Rev.* **2016**, *116*, 11877.
[8] J.-L. Bayo-Monton, A. Martinez-Millana, W. Han, C. Fernandez-Llatas, Y. Sun, V. Traver, *Sensors* **2018**, *18*, 1851.
[9] M. Khatib, H. Haick, *ACS Nano* **2022**, *16*, 7080.
[10] W. Gao, S. Emaminejad, H. Y. Y. Nyein, S. Challa, K. Chen, A. Peck, H. M. Fahad, H. Ota, H. Shiraki, D. Kiriya, *Nature* **2016**, *529*, 509.
[11] J. H. Lee, J. S. Heo, Y. J. Kim, J. Eom, H. J. Jung, J. W. Kim, I. Kim, H. H. Park, H. S. Mo, Y. H. Kim, *Adv. Mater.* **2020**, *32*, 2000969.
[12] a) W. Wu, H. Haick, *Adv. Mater.* **2018**, *30*, 1705024; b) A. Chortos, J. Liu, Z. Bao, *Nat. Mater.* **2016**, *15*, 937; c) D. H. Ho, Q. Sun, S. Y. Kim, J. T. Han, D. H. Kim, J. H. Cho, *Adv. Mater.* **2016**, *28*, 2601; d) T.-P. Huynh, M. Sosnowska, J. W. Sobczak, C. B. Kc, V. N. Nesterov, F. D'Souza, W. Kutner, *Anal. Chem.* **2013**, *85*, 8361; e) N. T. Tien, S. Jeon, D. I. Kim, T. Q. Trung, M. Jang, B. U. Hwang, K. E. Byun, J. Bae, E. Lee, J. B. H. Tok, *Adv. Mater.* **2014**, *26*, 796; f) G. Y. Bae, J. T. Han, G. Lee, S. Lee, S. W. Kim, S. Park, J. Kwon, S. Jung, K. Cho, *Adv. Mater.* **2018**, *30*, 1803388; g) C. M. Boutry, M. Negre, M. Jorda, O. Vardoulis, A. Chortos, O. Khatib, Z. Bao, *Sci. Rob.* **2018**, *3*, eaau6914; h) M. Zhang, J. J. Sun, M. Khatib, Z.-Y. Lin, Z.-H. Chen, W. Saliba, Y. D. Horev, V. Kloper, Y. Milyutin, T.-P. Huynh, *Nat. Commun.* **2019**, *10*, 1120; i) M. Khatib, T. P. Huynh, J. J. Sun, T. T. Do, P. Sonar, F. Hinkel, K. Müllen, H. Haick, *Adv. Funct. Mater.* **2019**, *29*, 1808188; j) M. Khatib, T. P. Huynh, Y. Deng, Y. D. Horev, W. Saliba, W. Wu, H. Haick, *Small* **2019**, *15*, 1803939.
[13] a) Q. Hua, J. Sun, H. Liu, R. Bao, R. Yu, J. Zhai, C. Pan, Z. L. Wang, *Nat. Commun.* **2018**, *9*, 244; b) M. Khatib, O. Zohar, W. Saliba, H. Haick, *Adv. Mater.* **2020**, *32*, 2000246.
[14] L. T. Duy, T. Q. Trung, V. Q. Dang, B. U. Hwang, S. Siddiqui, I. Y. Son, S. K. Yoon, D. J. Chung, N. E. Lee, *Adv. Funct. Mater.* **2016**, *26*, 4329.
[15] a) M. K. Nakhleh, Y. Y. Broza, H. Haick, *Nanomedicine* **2014**, *9*, 1991; b) U. Tisch, H. Haick, *MRS Bull.* **2010**, *35*, 797.
[16] R. S. Andre, R. C. Sanfelice, A. Pavinatto, L. H. Mattoso, D. S. Correa, *Mater. Des.* **2018**, *156*, 154.
[17] a) E. P. Ollé, J. Farré-Lladós, J. Casals-Terré, *Sensors* **2020**, *20*, 5478; b) G. Rebordão, S. I. Palma, A. C. Roque, *Sensors* **2020**, *20*, 5742.
[18] Z. Li, K. S. Suslick, *Acc. Chem. Res.* **2020**, *54*, 950.
[19] I.-S. Kang, H.-M. So, G.-S. Bang, J.-H. Kwak, J.-O. Lee, C. W. Ahn, *Appl. Phys. Lett.* **2012**, *101*, 123504.
[20] M. C. Janzen, J. B. Ponder, D. P. Bailey, C. K. Ingison, K. S. Suslick, *Anal. Chem.* **2006**, *78*, 3591.
[21] a) D. Zhang, J. Tong, B. Xia, *Sens. Actuators, B* **2014**, *197*, 66; b) D. Zhang, Z. Xu, Z. Yang, X. Song, *Nano Energy* **2020**, *67*, 104251; c) D. Zhang, H. Chang, P. Li, R. Liu, Q. Xue, *Sens. Actuators, B* **2016**, *225*, 233.
[22] a) S. Ampornpun, S. Montha, G. Tumcharern, V. Vchirawongkwin, M. Sukwattanasinitt, S. Wacharasindhu, *Macromolecules* **2012**, *45*, 9038; b) X. Qian, B. Städler, *Chem. Mater.* **2019**, *31*, 1196.
[23] D. MacLaren, M. A. White, *J. Mater. Sci.* **2005**, *40*, 669.